# nature geoscience

**Article** 

https://doi.org/10.1038/s41561-023-01324-x

# A hydrogen-enriched layer in the topmost outer core sourced from deeply subducted water

Received: 9 March 2023

Accepted: 11 October 2023

Published online: 13 November 2023



Check for updates

Taehyun Kim 1,2, Joseph G. O'Rourke 2, Jeongmin Lee 1, Stella Chariton, Vitali Prakapenka<sup>3</sup>, Rachel J. Husband<sup>4</sup>, Nico Giordano © <sup>4</sup>, Hanns-Peter Liermann **©**<sup>4</sup>, Sang-Heon Shim **©**<sup>2</sup> ⋈ & Yongjae Lee **©**<sup>1</sup> ⋈

The Earth's core-mantle boundary presents a dramatic change in materials, from silicate to metal. While little is known about chemical interactions between them, a thin layer with a lower velocity has been proposed at the topmost outer core (E'layer) that is difficult to explain with a change in concentration of a single light element. Here we perform high-temperature and-pressure laser-heated diamond-anvil cell experiments and report the formation of SiO<sub>2</sub> and FeH<sub>x</sub> from a reaction between water from hydrous minerals and Fe-Si alloys at the pressure-temperature conditions relevant to the Earth's core-mantle boundary. We suggest that, if water has been delivered to the core-mantle boundary by subduction, this reaction could enable exchange of hydrogen and silicon between the mantle and the core. The resulting H-rich, Si-deficient layer formed at the topmost core would have a lower density, stabilizing chemical stratification at the top of the core, and a lower velocity. We suggest that such chemical exchange between the core and mantle over gigayears of deep transport of water may have contributed to the formation of the putative E'layer.

Seismic studies have shown that the density of the Earth's outer core is ~10% lower than that of pure iron–nickel alloy<sup>1</sup>. In order to explain such a density deficit, substantial amounts of light elements are required in the core. Although the exact make-up of the light elements in the Earth's core is still debated<sup>2</sup>, silicon has been proposed as an important candidate<sup>3,4</sup>. However, the density deficit in the Earth's core cannot be explained by Si alone<sup>2,3,5</sup>.

Hydrogen has also been considered as a potential light element in the core because it becomes increasingly the siderophile element with pressure<sup>6</sup>. Hydrogen also strongly favours metallic liquid over silicate melt, suggesting large partitioning of Hinto the iron alloy during core formation<sup>7</sup>. For H in the core, it is also important to consider possible deep transport of water (or hydrogen) to the core-mantle boundary (CMB) region. Since the onset of plate tectonics, water could have been delivered to the deep mantle through subducting slabs<sup>8</sup>. Studies suggest that low-temperature subduction might have started between 2.0 and 2.5 Gyr ago<sup>9,10</sup> and the amount of subducted water from the surface is estimated to be  $\sim 10^{12} \, \text{kg yr}^{-1}$  (refs. 11,12).

Most water in the subducting slab is cycled back to the surface via the breakdown of hydrous (that is, water-containing) minerals by shallow-to-intermediate depths of ca. 300 km (ref. 12). However, some recently discovered dense hydrous phases (for example, hydrous magnesium silicates, FeO<sub>2</sub>H<sub>x</sub>, δ-AlOOH and hydrous stishovite) that are stable at the pressure-temperature (P-T) conditions of the lower mantle may play an important role in the deep water transport<sup>13–16</sup>. Seismologic and geodynamic studies have shown that cold slabs could penetrate the mantle transition zone and accumulate at the bottom of the lower mantle<sup>17,18</sup>. Owing to a rapid increase in temperature in the D"

Department of Earth System Sciences, Yonsei University, Seoul, South Korea. 2School of Earth and Space Exploration, Arizona State University, Tempe, AZ, USA. 3Center for Advanced Radiation Sources, University of Chicago, Argonne, IL, USA. 4Deutsches Elektronen-Synchrotron (DESY), Hamburg, Germany. e-mail: SHDShim@asu.edu; yongjaelee@yonsei.ac.kr

region, the temperature may reach a sufficient level for the dehydration of the stable hydrous phases<sup>14,19</sup>. The released water can then induce reactions between mantle and core materials at the CMB.

At the mantle side of the CMB, strong lateral variations in seismic properties have been identified<sup>20</sup>, suggesting chemical heterogeneities in the region. While subducted materials may be responsible for some of the structures<sup>21</sup>, in situ formation of chemical heterogeneities at the CMB has also been proposed<sup>22,23</sup>. For the outer core side, a thin low-velocity layer, labelled as E', has been documented in seismology<sup>24,25</sup>. While the observation has been debated<sup>26</sup>, the most recent study from both body-wave and normal-mode data favours the existence of a low-velocity layer at the outermost core<sup>25,27</sup>.

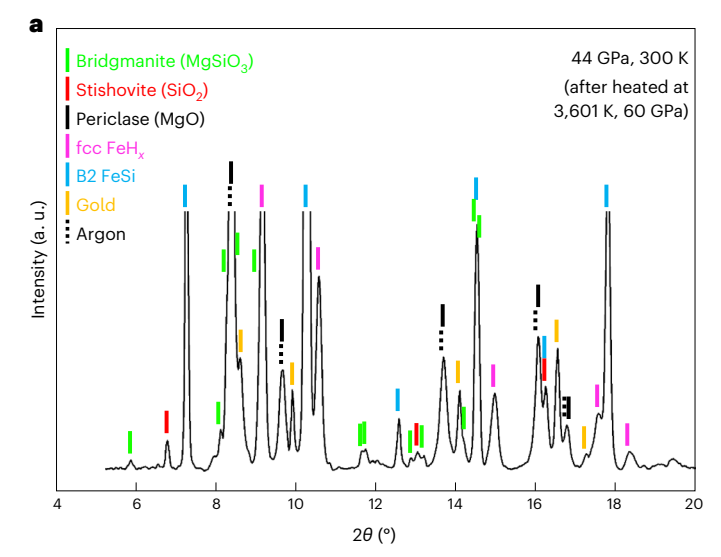
Given the fact that the putative E'layer exists near the contacting interface with the lowermost mantle, a gradient in light element concentration has been considered as an explanation for its origin (for example, refs. 28,29). However, the seismic observation and dynamic stability of the E'layer are difficult to satisfy simultaneously by an increase in the concentration of a single light element, as this would increase the velocity while decreasing the density<sup>30</sup>. As a plausible explanation, reducing the concentration of one light element while increasing another has been suggested<sup>30</sup>. Such an exchange process is, however, currently unknown to our knowledge.

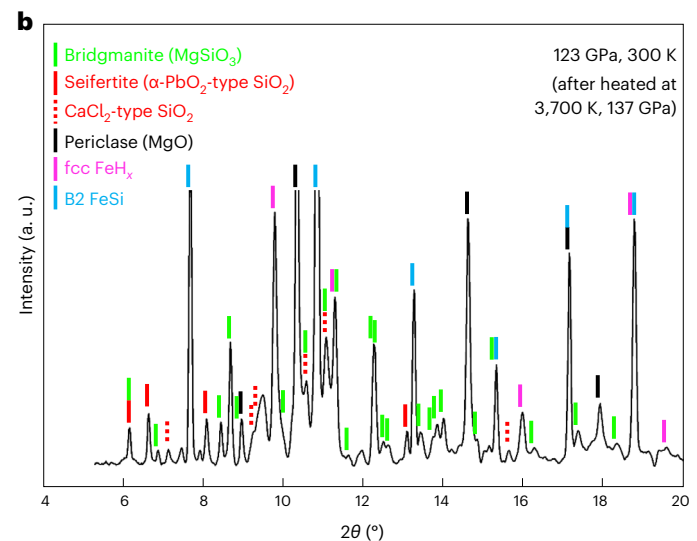
As hydrogen is an important component of deeply subducted materials while silicon is considered as an important light element in the core, processes involving these elements at the CMB region could shed new insights into the origin of the E'layer. Here, we report chemical reaction between Fe–Si alloys and hydrous minerals up to 137 GPa and ~4,000 K. Our observed reaction points to an exchange of Si and H between the mantle and the core. We also discuss how such chemical exchange could lead to in situ generation of chemical heterogeneities at both sides of the CMB.

### Reaction between water and Fe-Si alloys

As a simplified system, Fe-Si alloys were heated in a water medium to temperatures between 1,202 and 2,650 K at 20-32 GPa (Methods). During heating, the Fe-Si alloys were completely converted to stishovite (SiO<sub>2</sub>) and a face-centred cubic (fcc) form of FeH<sub>x</sub> (fcc FeH<sub>x</sub>; Extended Data Fig. 1a). When a limited amount of H<sub>2</sub>O (2 or 8 wt%, as controlled by Mg(OH)<sub>2</sub>) was present, Mg(OH)<sub>2</sub> breaks down to MgO and H<sub>2</sub>O, and H<sub>2</sub>O reacts subsequently with Fe-Si alloys (FeSi or Fe-9wt%Si) at higher P-T conditions up to 137 GPa and 3.700 K to form dense polymorphs of SiO<sub>2</sub>, the lower-mantle magnesium silicate phases and fcc FeH<sub>2</sub> (Fig. 1a,b). For example, after heating to 3,601 K at 60 GPa, bridgmanite (MgSiO<sub>3</sub>) and periclase (MgO) formed together with stishovite and fcc FeH<sub>x</sub> (Fig. 1a). Between 2,810 and 3,700 K in the 129–137 GPa range, we observed changes in the reaction products from the transformations of stishovite to the CaCl<sub>2</sub>-type phase and then to seifertite ( $\alpha$ -PbO<sub>2</sub>-type) phase<sup>31</sup>. Bridgmanite coexisting with post-perovskite<sup>32</sup> was observed at the highest P-T conditions of this study (Supplementary Table 1).

For a more realistic composition for the lower mantle, a hydrous silicate mixture of partially dehydrated lizardite and enstatite (MgSiO<sub>3</sub>) for a bulk composition of 44.3 wt% MgO, 54.0 wt% SiO<sub>2</sub> and 1.7 wt% H<sub>2</sub>O was used for reaction with Fe-9wt%Si. During heating above 3,000 K at 130-135 GPa, the seifertite-type SiO<sub>2</sub> and FeH, were observed (for example, run A12D\_32) (Fig. 1c for after quench, A12D\_34), consistent with the results from the simplified system discussed above. The diffraction peaks of bridgmanite or post-perovskite were also observed with enhanced diffraction intensity due to the use of a hydrous magnesium silicate as the starting sample (Fig. 1c and Extended Data Fig. 1b). We also examined a hydrous aluminous silicate system, that is, a mixture of Al(OH)<sub>3</sub> and MgSiO<sub>3</sub> for a bulk composition of 38.0 wt% MgO,  $56.8 \text{ wt}\% \text{SiO}_2$ ,  $3.4 \text{ wt}\% \text{Al}_2\text{O}_3$  and  $1.8 \text{ wt}\% \text{H}_2\text{O}$ . The starting material was heated together with Fe-9wt%Si at 110 GPa. We observed NiAs-type SiO<sub>2</sub> (refs. 33,34) as an oxidation product from Fe-9wt%Si, and fcc FeH $_x$  (or its melt) as the major iron phase above 3,500 K (Extended Data Fig. 1c





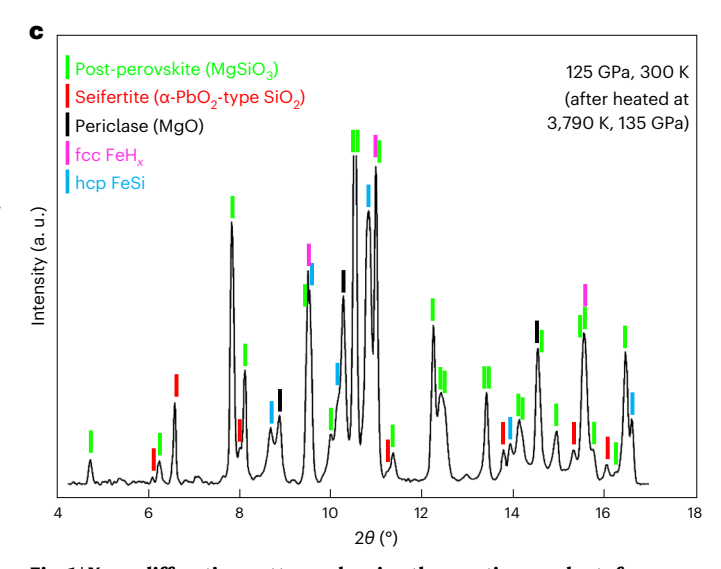


Fig. 1 | X-ray diffraction patterns showing the reaction products from three different sample setups. a-c, Fe-Si alloys with Mg(OH) $_2$  (a,b) and hydrous silicate (c). Data in a were collected at 44 GPa and 300 K quenched from 3,601 K and 60 GPa (A30B $_2$ 38), in b at 123 GPa and 300 K quenched from 3,700 K and 137 GPa (A15G $_2$ 30), and in c at 125 GPa and 300 K quenched from 3,790 K and 135 GPa (A12D $_2$ 34). The X-ray energy was 37 keV. The coloured vertical bars indicate the positions of the diffraction peaks from the identified phases.

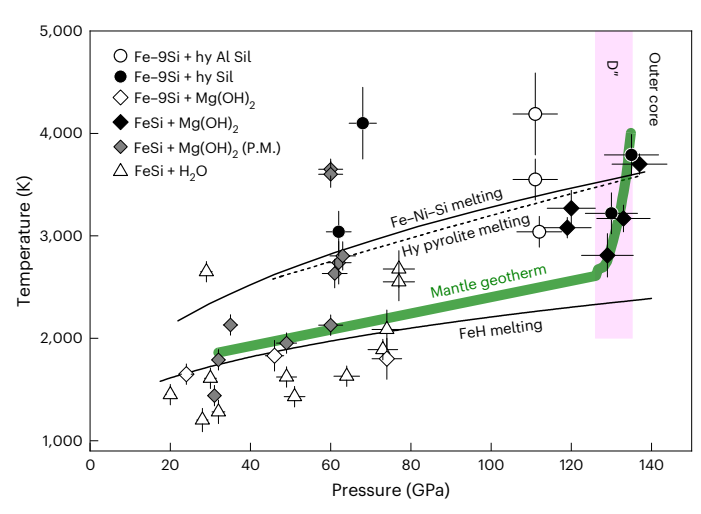


Fig. 2 | The pressure and temperature conditions of the reaction between Fe–Si alloys with different  $H_2O$  sources, including hydrous silicate, hydrous aluminous silicate,  $Mg(OH)_2$  and  $H_2O$ . A mantle geotherm  $^{59}$  (green solid curve) and the melting temperatures for Fe–Ni–Si $^{50}$ , FeH $^{37}$  (solid lines) and hydrous pyrolite  $^{61}$  (dashed line) are shown. A small increase in the geotherm near 126 GPa reflects the exothermic formation of post-perovskite  $^{59}$ . hy, hydrous; hy Al Sil, Al(OH) $_3$  + MgSiO $_3$ ; hy Sil, partially dehydrated lizardite + MgSiO $_3$ ; P.M., powdered FeSi and Mg(OH) $_2$  mixture as a starting material. The error bars for pressure are estimated to be  $\pm$  5%. Temperature uncertainties are estimated for  $1\sigma$ .

and Supplementary Table 1). Up to the P–T conditions of the CMB (Fig. 2), Our experiments thus consistently reveal the reaction between Fe–Si alloys and hydrous mantle compositions to produce dense  $SiO_2$  phases and  $FeH_x$  (Fig. 1 and Extended Data Figs. 1 and 2).

The unit-cell volume of the fcc phase is systematically larger than that of pure Fe metal over the entire P-T range of our experiments, suggesting the formation of FeH<sub>x</sub> (Extended Data Fig. 3 and Supplementary Table 2). The magnitude of the volume expansion in FeH, is, in the cases reacted with  $H_2O$  or  $Mg(OH)_2$ , consistent with x = 1 (refs. 35,36). When reacted with hydrous silicate or hydrous aluminous silicate with limited amounts of  $H_2O$ , the volume expansion of the fcc phase indicated x < 1in FeH<sub>y</sub>. There are two potential explanations for this observation: (1) the H<sub>2</sub>O amount in the starting materials is not sufficient; and (2) some H partitions into SiO<sub>2</sub>. When the reaction products were quenched from at least 1,000 K above the expected melting temperature of fcc FeH<sub>x</sub> (ref. 37), the volume of fcc FeH, becomes larger than those quenched from temperatures below the melting of fcc FeH, (Extended Data Fig. 3), which is explained by higher H solubility in molten Fe metal<sup>38</sup> (Supplementary Text 1). The unit-cell volume of the FeSi alloy is consistent with those of H-free cases, suggesting no significant hydrogenation of the alloy (Extended Data Fig. 4).

By employing focused ion beam and electron microscopy, we studied the structure and chemistry of the recovered samples (Fig. 3 and Extended Data Figs. 5–8). Figure 3a–c shows the reaction products from the homogeneous mixture of FeSi and Mg(OH), (2 wt% H<sub>2</sub>O) recovered from 2,632 K and 61 GPa. As this P-T condition is above the melting temperature of FeH<sub>x</sub>, a metallic melt pocket was formed at the heating centre. The Si content increases towards the boundary with Mg-silicate/oxide phases (Fig. 3b). Inside the metallic melt pocket, sub-micrometre-sized pores are distributed with their sizes decreasing towards the boundary (Fig. 3c). Such a structure can form from hydrogen escape from FeH<sub>x</sub> (and its higher H concentration in the hottest central region) during decompression<sup>39,40</sup>. In the water-saturated runs, little Si was found in metallic melt due to more extensive reaction (Fig. 3d). Similar chemical separations are also observed in the samples recovered from P-T conditions relevant to the CMB (Fig. 3e,f). The morphology of the metallic melt in the heating spot (Fig. 3e), however,

differs from the sample quenched from 61 GPa (Fig. 3a) because a different sample configuration was adopted for the CMB run where a separate FeSi layer was in contact with two sandwiching Mg(OH)<sub>2</sub> layers. These observations are consistent with our X-ray diffraction (XRD) results (Figs. 1 and 3).

Because the starting materials did not contain any free silica phases, the silicate regions found in the recovered samples in electron microscopy must have formed by silicon oxidized from the Fe-Si alloy. In the starting mixture with hydrous silicate, SiO<sub>2</sub> was found at the boundary between metallic melt and silicate melt (Extended Data Fig. 7), supporting that SiO<sub>2</sub> was formed by the reaction rather than possible breakdown of silicate. For the samples heated with Mg(OH)<sub>2</sub>, a homogeneous mixture of low-Fe bridgmanite [(Mg<sub>0.99</sub>,Fe<sub>0.01</sub>)SiO<sub>3</sub>] and ferropericlase [(Mg<sub>0.99</sub>,Fe<sub>0.01</sub>)O] was found at the heated spot (Fig. 3b, f and Supplementary Table 3). Alocal equilibrium was probably established because both the Mg-silicate/oxide and metallic regions were in contact at (partially) molten conditions during heating. The sample also enabled us to infer the redox conditions of the heated spots (Methods). The oxygen fugacity (fO<sub>2</sub>) of the two different heated spots shown in Fig. 3a,e were 4 log units below the iron-wüstite (IW) buffer (Supplementary Table 3). Studies have estimated at least 2 log units below the IW buffer for the fO<sub>2</sub> of the deep mantle<sup>41</sup>. We found that sufficient heating at high temperature is the key to achieve local equilibrium (Extended Data Fig. 5 and Supplementary Text 2).

# Possible effects of H and Si exchange at the CMB conditions

Our experiments show that water from hydrous minerals reacts with Fe–Si alloys at the pressure, temperature and redox conditions relevant for the Earth's deep interior. The reaction hydrogenates the Fe-rich liquid while oxidizing Si to form silica (Fig. 1 and Extended Data Fig. 1). In this reaction, the amount of H<sub>2</sub>O required for oxidizing Si can be constrained through a redox reaction: Si<sup>0</sup> (metal) +  $2H_2O \rightarrow 4H^0$  (metal) +  $SiO_2$ . The amount of H alloyed with Fe metal can also be estimated.

Although hydrogen could have been incorporated into the core during the early processes<sup>7</sup> (Supplementary Text 3), it is feasible that subducting slabs have supplied a significant amount of hydrogen (or water) to the CMB region over an extended period (Fig. 4a). Recent high-pressure studies have found some hydrous phases stable in the subducting slabs in the lower mantle, although some water loss at the 660-km discontinuity seems to be inevitable due to the changes in the water storage capacity<sup>42</sup>. While there are many factors to be considered for the estimation of the amount of water delivered to the CMB (to participate in the reaction), the fraction of the total subducted water transported to the CMB and its duration are important (Fig. 4b). Although these two parameters are uncertain, if 1% of the total subducted water (that is,  $10^{12} \, kg \, yr^{-1} \times 0.01$ ; ref. 12) can be delivered to the core, approximately  $10^{18}\,\mathrm{kg}$  of hydrogen could have been supplied since 2.5 Gyr ago<sup>9</sup>, assuming no major changes in subduction style. If the water delivered to the CMB as a component of hydrous minerals is released by dehydration and reacts with the core material as we observed here, H could be incorporated into the outer core, while Si in the outer core could be oxidized (that is, SiO<sub>2</sub>) and released to the mantle (Fig. 4a). The extracted silica from the core may not exist as a free phase at the CMB region, but probably reacts with ferropericlase to form bridgmanite or post-perovskite, as observed in some of our experiments (Figs. 1 and 3, and Extended Data Figs. 1, 6 and 7).

Because hydrogen has a relatively large effect on the density of iron alloys, the chemical reaction identified in our experiments could create chemical stratification at the top of the core (Fig. 4a). Flows associated with thermal (or thermochemical) convection in the rest of the outer core are not strong enough to erode such a stable layer, even over geologic time<sup>43</sup>. While mixing hydrogen throughout the entire core would require a huge amount of energy to counteract its buoyancy,

accumulating hydrogen into a stable layer does not challenge the bulk energetics of the geodynamo. However, such a stable layer could affect the structure of the magnetic field observed at the surface and appear in seismic data. Indeed, several studies support the existence of a stable layer at the top of the core based on anomalously slow seismic wave speeds  $^{24,44}$  as well as geomagnetic observations and simulations (for example, refs. 45-47). However, these studies predict different properties for the stable layer (for example, thickness between 60 and 400 km with varying degrees of stability). Other works argue that a stable layer is not the sole option to explain the available observations, but also should not be excluded (for example, refs. 26,48).

To assess the range of possibilities, we computed the Brunt-Väisälä period  $(T_{\rm RV})$  of a layer with an assumed thickness and extra mass of hydrogen to assess its stability (Methods). Lower values of  $T_{\rm BV}$  represent stronger stratification. Although Si is removed from the core, the resulting metallic liquid is still buoyant with respect to the bulk core because H is added<sup>49</sup>. Transferring ca. 2.7 × 10<sup>18</sup> kg H (Supplementary Table 4 and Methods) into the core (and removing the associated amount of Si) could produce a stable layer with a thickness of 400 km and  $T_{\rm BV} \approx 48$  hours, in agreement with ref. 45. Even less H (ca.  $1.2 \times 10^{18}$  kg) is required to produce a stable layer with a thickness of ca. 130 km and  $T_{\rm BV} \approx 24$  hours as estimated by ref. 50 (Fig. 4c). The amount of hydrogen required to explain these existing models corresponds to  $1-2 \times 10^{19}$  kg H<sub>2</sub>O delivered to the CMB, which is well within the range we estimate that subduction delivered (Fig. 4b and Supplementary Table 4). Producing the most stable and thick layer (that is, ca. 300 km thick,  $T_{\rm BV} \approx 1.6-3.4$  hours), compatible with ref. 44, with subduction processes alone, however, would need at least ca.  $4.0 \times 10^{20}$  kg H (that is,  $>3 \times 10^{21}$  kg H<sub>2</sub>O), which would require a deep water cycle with an unrealistic efficiency of more than 90%.

Over a few decades, attempts have been made to explain a possible low-velocity layer in the topmost outer core (the E'layer) with light element enrichment and/or thermal stratification. However, as pointed out by ref. 30, no single light element enrichment can satisfy both the low-density and low-velocity requirement for the observed stable E' layer at the topmost core.

The experimental results we present here point to a core-mantle chemical exchange process between H in the lower mantle and Si in the topmost outer core. According to the data in ref. 51, an increase of ~1 wt% H can increase the P-wave velocity (Vp) by ~5.1% at 150 GPa and 4.000 K. Ref. 5 showed that removing ~1 wt% of Si would decrease Vp. by ~2.7%. We assume that P-wave velocity (ΔVp) changes linearly with the amounts of H and Si. The chemical reaction found in this study indicates  $-7 \times \Delta m(H) = \Delta m(Si)$ , where  $\Delta m(H)$  and  $\Delta m(Si)$  are mass fraction changes of light elements in the outermost core (Methods). The mass of the topmost 100 km region of the outer core is  $\sim 1.5 \times 10^{23}$  kg. Adding  $2-3 \times 10^{18}$  kg H thus corresponds to  $\Delta m(H) \approx 1.4 \times 10^{-3}$  to  $2.0 \times 10^{18}$  $10^{-3}$  wt% and  $\Delta m(Si) \approx -9.8 \times 10^{-3}$  to  $-1.4 \times 10^{-2}$  wt% (Methods and Supplementary Table 4). The net effect is to decrease the P-wave velocity by 0.02 to 0.03%. In addition, we used the parameters and methods in ref. 52, which included the combined effects of Si and H on the velocity. For the same H increase and Si decrease, this independent estimation results in a ~0.01% decrease in bulk sound velocity of Fe-Si-H alloy (Methods), consistent with the estimation above based on a linear assumption.

Seismic models estimated the maximum velocity decrease of 0.1–0.3% at the topmost outer core, while the velocity decrease fades to -0% at a depth of -100–400 km from the CMB<sup>44,53,54</sup>. Therefore, the average velocity decrease predicted by our model is smaller than the maximum predicted by the seismic models for the E'layer. For more realistic comparisons, however, it is important to improve constraints on the following: (1) velocity changes of iron alloy liquid for different combinations of light elements (for example, study of liquid Fe–Si–H ternary system at the outer core conditions); (2) depth-dependent changes in the concentrations of H and Si at the top of the outer core;

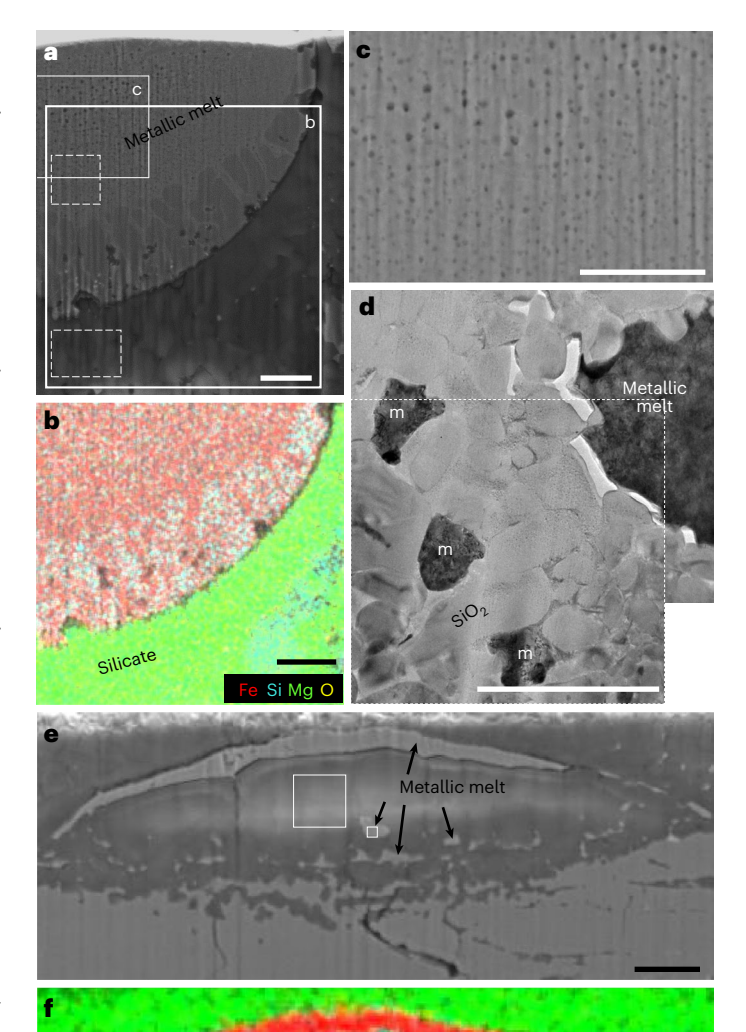
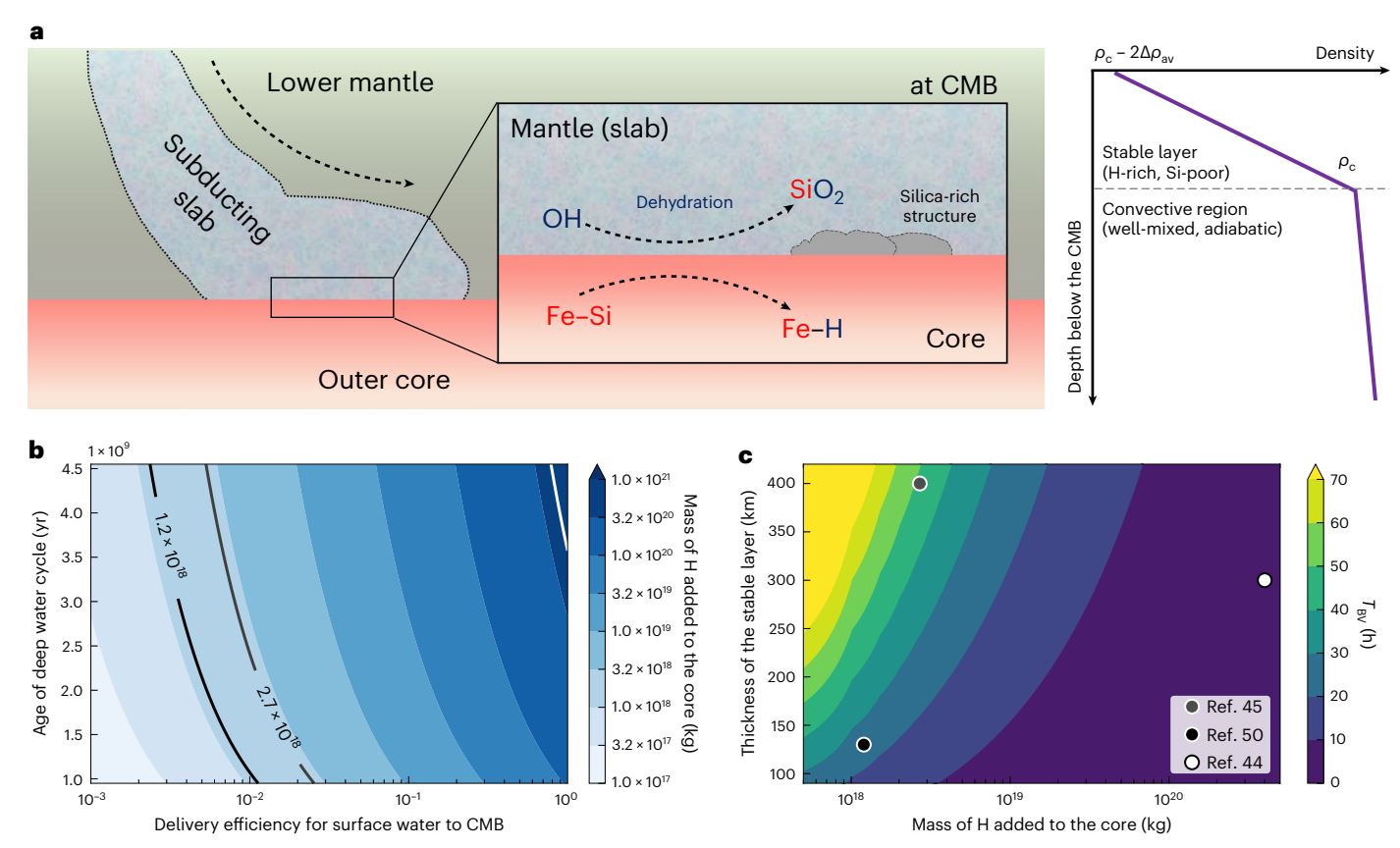


**Fig. 3** | **SEM and TEM images of the recovered samples. a**, A cross-sectional view of the recovered sample from a mixture of FeSi + Mg(OH)<sub>2</sub> in an Ar medium (setup 2 in Supplementary Table 1) after heating at 2,632 K at 61 GPa (A30B\_40). EDS was measured at two locations, indicated by dashed white boxes for the quenched metallic (upper) and silicate (lower) melts (Supplementary Table 3). **b**, The elemental distribution map for the region indicated by the large solid white box (b) in **a. c**, The porous texture in the centre of the metallic melt for the smaller white solid boxed area (c) in **a. d**, A representative TEM image of the heated spots shown in Extended Data Fig. 8 (A30A\_14). Two TEM images were combined at the dotted white line. m, metallic melt. **e**, A cross-sectional view of the recovered sample from FeSi sandwiched between two Mg(OH)<sub>2</sub> layers after heating at 3,700 K at 137 GPa (A15G\_28). EDS was performed at two locations indicated by white boxes for the quenched metallic melt (smaller box) and silicate (larger box) regions (Supplementary Table 3). **f**, The elemental distribution map of Fe (red), Si (cyan) and Mg (green) for **e**. Scale bars, 1 μm.

and (3) the depths and the magnitude of the velocity decrease in the E' layer. In addition to the H-Si exchange process we propose here, other processes could cause velocity and density anomalies, such as chemical exchange between oxygen and silicon (for example, refs. 29,55),



 $\label{eq:Fig.4} Fig. 4 | Proposed chemical exchange at the CMB and its effect on the evolution of the Earth's topmost outer core. a, Schematic drawing outlining the chemical exchange reaction processes in the Fe-Si-O-H system in the CMB region (left). Schematic plot for a density profile induced by the chemical reaction at the CMB (right). b, Delivered mass of H (to the core) as a function of the fraction of total subducted water and duration of water delivery. The white contour line is for$ 

 $4.0 \times 10^{20}$  kg. **c**, The thickness of stable layer and its  $T_{\rm BV}$  for the H amount needed to sustain the layer without any other chemical reactions or sub-adiabatic heat flow.  $\rho_{\rm c}$ , density of the core;  $\rho_{\rm av}$ , average density in the stable layer. Note that a wide range of H mass (delivered to the core) could explain the previous studies  $^{44,45,50}$  for the thickness of stable layer at the top of outer core. The grey, black and white circles in **c** correspond to the matching H mass contours in **b**.

sub-adiabatic heat flow across the CMB (for example, ref. 56) and lateral variations in the heat flux (for example, ref. 57). Furthermore, input of H from the mantle may induce stratification by immiscible liquids such as Fe–H and Fe–S<sup>58</sup>.

As shown here, the H–Si chemical exchange process promoted by subducted water at the CMB could explain the seismic properties (at least qualitatively) and at the same time satisfy the lower density requirement for the dynamic stability of the putative E′layer. While more studies are desirable, our study reveals the intriguing possibility that the E′layer is the consequence of deep transport of subducted surface water over gigayears of the deep hydrogen cycle. Therefore, our model presented here shows that the mantle and the core systems are not chemically separated over the geological timescale, but they may have exchanged some elements even after their differentiations in the early Earth.

# Online content

Any methods, additional references, Nature Portfolio reporting summaries, source data, extended data, supplementary information, acknowledgements, peer review information; details of author contributions and competing interests; and statements of data and code availability are available at https://doi.org/10.1038/s41561-023-01324-x.

### References

 Dziewonski, A. M. & Anderson, D. L. Preliminary reference Earth model. Phys. Earth Planet. Inter. 25, 297–356 (1981).

- 2. Hirose, K. et al. Composition and state of the core. *Annu. Rev. Earth Planet. Sci.* **41**, 657–691 (2013).
- Badro, J. et al. A seismologically consistent compositional model of Earth's core. Proc. Natl Acad. Sci. USA. 111, 7542–7545 (2014).
- Rubie, D. C. et al. Accretion and differentiation of the terrestrial planets with implications for the compositions of early-formed Solar System bodies and accretion of water. *Icarus* 248, 89–108 (2015).
- Nakajima, Y. et al. Silicon-depleted present-day Earth's outer core revealed by sound velocity measurements of liquid Fe–Si alloy. J. Geophys. Res. Solid Earth 125, e2020JB019399 (2020).
- Badding, J. V. et al. High-pressure chemistry of hydrogen in metals: in situ study of iron hydride. Science 253, 421–424 (1991).
- 7. Tagawa, S. et al. Experimental evidence for hydrogen incorporation into Earth's core. *Nat. Commun.* **12**, 2588 (2021).
- 8. Holland, G. & Ballentine, C. J. Seawater subduction controls the heavy noble gas composition of the mantle. *Nature* **441**, 186–191 (2006).
- Martin, H. Effect of steeper Archean geothermal gradient on geochemistry of subduction-zone magmas. *Geology* 14, 753–756 (1986).
- van Hunen, J. & Moyen, J.-F. Archean subduction: fact or fiction? Annu. Rev. Earth Planet. Sci. 40, 195–219 (2012).
- Bekaert, D. V. et al. Subduction-driven volatile recycling: a global mass balance. Annu. Rev. Earth Planet. Sci. 49, 37–70 (2021).

- van Keken, P. E. et al. Subduction factory: 4. Depth-dependent flux of H<sub>2</sub>O from subducting slabs worldwide. *J. Geophys. Res.* 116. B01401 (2011).
- Pamato, M. G. et al. Lower-mantle water reservoir implied by the extreme stability of a hydrous aluminosilicate. *Nat. Geosci.* 8, 75–79 (2015).
- 14. Nishi, M. et al. The pyrite-type high-pressure form of FeOOH. *Nature* **547**, 205–208 (2017).
- Nishi, M. et al. Stability of hydrous silicate at high pressures and water transport to the deep lower mantle. *Nat. Geosci.* 7, 224–227 (2014).
- Lin, Y. et al. Evidence for the stability of ultrahydrous stishovite in Earth's lower mantle. Proc. Natl Acad. Sci. USA 117, 184–189 (2020).
- Niu, Y. Origin of the LLSVPs at the base of the mantle is a consequence of plate tectonics – a petrological and geochemical perspective. Geosci. Front. 9, 1265–1278 (2018).
- Sun, D. et al. Slab control on the northeastern edge of the mid-Pacific LLSVP near Hawaii. Geophys. Res. Lett. 46, 3142–3152 (2019).
- 19. Piet, H. et al. Dehydration of  $\delta$ -AlOOH in Earth's deep lower mantle. *Minerals* **10**, 348 (2020).
- 20. Yuan, K. & Romanowicz, B. Seismic evidence for partial melting at the root of major hot spot plumes. *Science* **357**, 393–397 (2017).
- Brandenburg, J. P. & van Keken, P. E. Deep storage of oceanic crust in a vigorously convecting mantle. J. Geophys. Res. 112, B06403 (2007).
- Manga, M. & Jeanloz, R. Implications of a metal-bearing chemical boundary layer in D" for mantle dynamics. Geophys. Res. Lett. 23, 3091–3094 (1996).
- 23. Li, M. et al. Compositionally-distinct ultra-low velocity zones on Earth's core–mantle boundary. *Nat. Commun.* **8**, 177 (2017).
- Garnero, E. J. et al. Constraining outermost core velocity with SmKS waves. Geophys. Res. Lett. 20, 2463–2466 (1993).
- Ma, X. & Tkalčić, H. CCMOC: a new view of the Earth's outer core through the global coda correlation wavefield. *Phys. Earth Planet. Inter.* 334, 106957 (2023).
- 26. Irving, J. C. E. et al. Seismically determined elastic parameters for Earth's outer core. Sci. Adv. 4, eaar2538 (2018).
- van Tent, R. et al. The signal of outermost-core stratification in body-wave and normal-mode data. *Geophys. J. Int.* 223, 1338– 1354 (2020).
- 28. Labrosse, S. et al. A crystallizing dense magma ocean at the base of the Earth's mantle. *Nature* **450**, 866–869 (2007).
- Davies, C. J. et al. Transfer of oxygen to Earth's core from a long-lived magma ocean. Earth Planet. Sci. Lett. 538, 116208 (2020).
- Brodholt, J. & Badro, J. Composition of the low seismic velocity E' layer at the top of Earth's core. Geophys. Res. Lett. 44, 8303–8310 (2017).
- 31. Grocholski, B. et al. Stability, metastability, and elastic properties of a dense silica polymorph, seifertite. *J. Geophys. Res. Solid Earth* **118**, 4745–4757 (2013).
- Tateno, S. et al. Determination of post-perovskite phase transition boundary up to 4400 K and implications for thermal structure in D" layer. Earth Planet. Sci. Lett. 277, 130–136 (2009).
- Nisr, C. et al. Large H<sub>2</sub>O solubility in dense silica and its implications for the interiors of water-rich planets. *Proc. Natl Acad. Sci. USA* 117, 9747–9754 (2020).
- Liu, L. et al. Formation of an Al-rich niccolite-type silica in subducted oceanic crust: implications for water transport to the deep lower mantle. Geophys. Res. Lett. 49, e2021GL097178 (2022).
- 35. Pépin, C. M. et al. New iron hydrides under high pressure. *Phys. Rev. Lett.* **113**, 265504 (2014).

- 36. Kato, C. et al. Stability of fcc phase FeH to 137 GPa. *Am. Mineral.* **105**. 917–921 (2020).
- Hirose, K. et al. Hydrogen limits carbon in liquid iron. Geophys. Res. Lett. 46, 5190–5197 (2019).
- 38. Piet, H. et al. Superstoichiometric alloying of H and close-packed Fe–Ni metal under high pressures: implications for hydrogen storage in planetary core. *Geophys. Res. Lett.* **50**, e2022GL101155 (2023).
- Okuchi, T. Hydrogen partitioning into molten iron at high pressure: implications for Earth's core. Science 278, 1781–1784 (1997).
- 40. lizuka-Oku, R. et al. Hydrogenation of iron in the early stage of Earth's evolution. *Nat. Commun.* **8**, 14096 (2017).
- 41. Frost, D. J. & McCammon, C. A. The redox state of Earth's mantle. *Annu. Rev. Earth Planet. Sci.* **36**, 389–420 (2008).
- 42. Walter, M. J. Water transport to the core-mantle boundary. *Natl Sci. Rev.* **8**, nwab007 (2021).
- Bouffard, M. et al. Convective erosion of a primordial stratification atop Earth's core. Geophys. Res. Lett. 47, e2020GL087109 (2020).
- Helffrich, G. & Kaneshima, S. Outer-core compositional stratification from observed core wave speed profiles. *Nature* 468, 807–810 (2010).
- Olson, P. et al. Outer core stratification from the high latitude structure of the geomagnetic field. Front. Earth Sci. 6, 140 (2018).
- 46. Buffett, B. Geomagnetic fluctuations reveal stable stratification at the top of the Earth's core. *Nature* **507**, 484–487 (2014).
- Yan, C. & Stanley, S. Sensitivity of the geomagnetic octupole to a stably stratified layer in the Earth's core. *Geophys. Res. Lett.* 45, 11005–11011 (2018).
- 48. Christensen, U. R. Geodynamo models with a stable layer and heterogeneous heat flow at the top of the core. *Geophys. J. Int.* **215**, 1338–1351 (2018).
- 49. Umemoto, K. & Hirose, K. Chemical compositions of the outer core examined by first principles calculations. *Earth Planet. Sci. Lett.* **531**, 116009 (2020).
- 50. Buffett, B. et al. Evidence for MAC waves at the top of Earth's core and implications for variations in length of day. *Geophys. J. Int.* **204**, 1789–1800 (2016).
- 51. Umemoto, K. & Hirose, K. Liquid iron–hydrogen alloys at outer core conditions by first-principles calculations. *Geophys. Res. Lett.* **42**, 7513–7520 (2015).
- 52. Fu, S. et al. Hydrogen and silicon effects on hexagonal close packed Fe alloys at high pressures: implications for the composition of Earth's inner core. *J. Geophys. Res. Solid Earth* **128**, e2022JB026016 (2023).
- Kaneshima, S. & Helffrich, G. Vp structure of the outermost core derived from analysing large-scale array data of SmKS waves. Geophys. J. Int. 193, 1537–1555 (2013).
- Tang, V. et al. Seismological evidence for a non-monotonic velocity gradient in the topmost outer core. Sci. Rep. 5, 8613 (2015).
- 55. Mittal, T. et al. Precipitation of multiple light elements to power Earth's early dynamo. Earth Planet. Sci. Lett. **532**, 116030 (2020).
- Nakagawa, T. On the thermo-chemical origin of the stratified region at the top of the Earth's core. Phys. Earth Planet. Inter. 276, 172–181 (2018).
- 57. Mound, J. et al. Regional stratification at the top of Earth's core due to core–mantle boundary heat flux variations. *Nat. Geosci.* **12**, 575–580 (2019).
- 58. Yokoo, S. et al. Stratification in planetary cores by liquid immiscibility in Fe-S-H. *Nat. Commun.* **13**, 644 (2022).
- Ono, S. Experimental constraints on the temperature profile in the lower mantle. *Phys. Earth Planet. Inter.* 170, 267–273 (2008).

- 60. Morard, G. et al. Melting of Fe–Ni–Si and Fe–Ni–S alloys at megabar pressures: implications for the core–mantle boundary temperature. *Phys. Chem. Miner.* **38**, 767–776 (2011).
- 61. Nomura, R. et al. Low core–mantle boundary temperature inferred from the solidus of pyrolite. *Science* **343**, 522–525 (2014).

**Publisher's note** Springer Nature remains neutral with regard to jurisdictional claims in published maps and institutional affiliations.

Springer Nature or its licensor (e.g. a society or other partner) holds exclusive rights to this article under a publishing agreement with the author(s) or other rightsholder(s); author self-archiving of the accepted manuscript version of this article is solely governed by the terms of such publishing agreement and applicable law.

@ The Author(s), under exclusive licence to Springer Nature Limited 2023

### Methods

#### Sample preparation

We used symmetric-type diamond-anvil cells, with diamond culet sizes ranging between 400 and 120  $\mu$ m to achieve pressures between 17 and 137 GPa. Rhenium gaskets were pre-indented to a thickness of 20–25  $\mu$ m and drilled to make a hole (with diameters between 250 and 60  $\mu$ m) as a sample chamber. Six different sample setups were prepared: (1) FeSi in a H<sub>2</sub>O medium; (2) a mixture of FeSi + Mg(OH)<sub>2</sub> in an argon (gas) or MgO (solid) medium; (3) an FeSi foil sandwiched between two Mg(OH)<sub>2</sub> layers; (4) an Fe–9wt%Si foil sandwiched between two Mg(OH)<sub>2</sub> layers; (5) an Fe–9wt%Si foil sandwiched between two hydrous silicate (a lizardite + MgSiO<sub>3</sub> enstatite mixture for 44.3 wt% MgO, 54.0 wt% SiO<sub>2</sub> and 1.7 wt% H<sub>2</sub>O) layers; and (6) an Fe–9wt%Si foil sandwiched between two hydrous aluminous silicate (an Al(OH)<sub>3</sub> + MgSiO<sub>3</sub> enstatite mixture for 38.0 wt% MgO, 56.8 wt% SiO<sub>2</sub>, 3.4 wt% Al<sub>2</sub>O<sub>3</sub> and 1.8 wt% H<sub>2</sub>O) layers.

For setup 2, we mixed a synthesized brucite (Sigma-Aldrich) with FeSi alloy (Alfa Aesar) to achieve 2 wt%  $\rm H_2O$ , which was ground in an agate mortar for 1 hour. The powdered sample was mixed with gold powder (Alfa Aesar) as a pressure standard, and cold-compressed to a respective thin foil (thickness of approximately 10  $\mu m$ ). The foil was loaded with 3–4 spacers of the same composition of mixture on each side of the diamond culet to separate the foil from the diamonds and to make space for argon as a gas medium. We used gas loading systems at GeoSoilEnviroCARS (GSECARS) or the Extreme Conditions Beamline to load the pressurized argon into the sample chamber.

In the cases of MgO or Mg(OH) $_2$  as a solid medium (setups 2, 3 or 4), FeSi or Fe–9wt%Si (Goodfellow) powders were cold-compressed to make a foil, and then it was sandwiched between two 3–5  $\mu$ m thick MgO or Mg(OH) $_2$  layers, which insulate Fe–Si alloys. For setups 3 and 4, from the thickness of the sample foils and Mg(OH) $_2$  layers, we estimate 7–9 wt% H $_2$ O. For setup 1, FeSi powder was cold-compressed to a thin foil as above. We followed the same sample preparation procedure as setup 2, except that deionized water (H $_2$ O) was loaded as a liquid medium instead.

For setup 5, we mixed synthetic lizardite<sup>62</sup>, a hydrous magnesium silicate (Mg<sub>3</sub>Si<sub>2</sub>O<sub>5</sub>(OH)<sub>4</sub>) and powdered natural enstatite (MgSiO<sub>3</sub>). Lizardite, one of the representative minerals in the serpentine group, forms from a hydrothermal alteration of mantle rocks (for example, peridotite) at various geological environments, including subduction zones<sup>63</sup>. To control the water content to be realistic for the (cold) subducting slabs into the deep mantle, the synthetic lizardite was partially dehydrated at 870 K in the thermogravimetric analyser instrument (LABSYS evo, Setaram Instrumentation). The partially dehydrated lizardite sample was mixed with the enstatite powder. Mixed powders were then ground using an agate mortar for 30 minutes for a homogeneous mixture. Similar to setups 3 and 4, Fe-9wt%Si foil was sandwiched between the two layers of the hydrous silicate mixture. For setup 6, Al(OH)<sub>3</sub> (Sigma-Aldrich) was mixed with MgSiO<sub>3</sub> instead of lizardite. For setups 1–6, the sample chamber was sealed during gas/liquid/ solid loading and then compressed to 10-15 GPa, which was further compressed to the target pressures at the beamline.

#### Synchrotron X-ray diffraction

X-ray diffraction patterns were collected in situ at high-pressure and high-temperature conditions using a double-sided laser-heating setup at beamline 13-IDD of the GSECARS at the Advanced Photon Source. A monochromatic X-ray beam (a wavelength of 0.3344(1) Å or 0.4133(1) Å) was focused to  $3\times 2$  µm in size using the canted undulator dual crystal monochromator, Kirkpatrick–Baez mirror and a pinhole. The pixel array detector (Pilatus 3 X CdTe 1 M) was used to obtain diffraction images. At beamline P02.2 (PETRA III) at Deutsches Elektronen-Synchrotron, monochromatic X-rays (a wavelength of 0.2887(1) Å or 0.2908(1) Å) were focused to  $1.9\times 1.9$  µm² or  $1.8\times 2.8$  µm² using Kirkpatrick–Baez mirrors and a pinhole, and a PerkinElmer

XRD 1621 flat-panel detector was used for collecting diffraction data. We used LaB<sub>6</sub> or CeO<sub>2</sub> standards to calibrate and correct for distortions and obtain sample-to-detector distances (ca. 200 mm or 400 mm).

For laser heating diamond-anvil cell (LH-DAC) experiments at the 13-IDD and PO2.2 beamlines, near-infrared lasers were focused on both sides of the sample foil in a LH-DAC to a hot spot size of 20-25  $\mu m$  and aligned coaxially with the X-ray <sup>64,66</sup>. We collected in situ X-ray diffraction data over a pressure range between 17 and 137 GPa. During laser heating, the temperature fluctuation was low ( $\pm 100$  K), including the conditions above the melting temperature of FeH (for example, A30B\_34 in Supplementary Table 1). X-ray diffraction patterns were mostly measured when the temperature fluctuation was less than 100-150 K. In a few heating runs, temperature fluctuation in the heating spots became higher than 150 K at temperatures above the melting of H<sub>2</sub>O or iron-rich alloys. In such cases, we collected diffraction data for less than 10 seconds at target temperatures to minimize the impact of temperature fluctuation during X-ray diffraction measurement.

The thermal radiation from both sides of the LH-DAC was measured using the optical spectroscopy system (at the above two beamlines), which is composed of dielectric laser mirrors, glassy carbon mirrors, apochromatic objective lenses, notch filters, laser dichroic mirrors and other optics. The thermal radiation is collected by a two-dimensional area charge-coupled device detector (for more details on the setup, see refs. 64,66). The measured spectra are corrected for system response, which is measured using a tungsten ribbon lamp with known radiance. The corrected spectra are then fitted to the grey-body radiation between 680 and 840 nm (see refs. 67,68 for more details on calibration). Temperatures were calculated using the T-Rax software package (https://github.com/CPrescher/T-Rax). Considering axial gradients, differences between the two sides of the LH-DAC and temperature fluctuations during the measurement, typical uncertainty in the measured temperature is  $\pm 100-200 \, \text{K}^{64,68,69}$ .  $Supplementary\,Table\,1\,lists\,our\,measured\,temperatures\,with\,estimated$  $1\sigma$  uncertainties.

Two-dimensional X-ray diffraction images were converted to one-dimensional X-ray diffraction patterns, using the Dioptas software Pessures were determined using the equation of state of gold We used the PeakPo software package for the peak identification and unit-cell fitting.

#### Chemical analysis

To gain further insights into the elemental partitioning at high pressures and high temperatures, we recovered the laser-heated samples after the in situ X-ray diffraction measurements and performed electron microscopy imaging and chemical analyses. We used a scanning electron microscope (SEM) combined with a focused (Ga<sup>+</sup>) ion beam (FIB) and energy dispersive X-ray spectroscopy (EDS). The recovered samples were coated with platinum (Pt) and sectioned using an FIB instrument (Crossbeam 540, ZEISS, at Yonsei University). We avoided parts of the samples contaminated during FIB milling. The cross-section of the samples was measured for the two-dimensional elemental mapping analysis at 5 keV and 15 keV, using EDS (Xflash 6 | 30 detector, Bruker) for Fe, Si, Mg and O, installed in the same FIB instrument. We also performed SEM-EDS analysis for a recovered sample using an FIB instrument (Helios 5 UX, Thermo Scientific) at Arizona State University. Distribution of Fe, Si and Mg were measured at 10 keV. After an examination of the elemental distribution of the laser-heated spots, for some samples, we selected an area that contains iron-rich melt and its surrounding part for transmission electron microscopy (TEM) analysis. For TEM (JEM F200, JEOL, at Yonsei University) analysis, the sample was further milled at 30 keV and 3 nA, and then extracted to mount on a copper (Cu) grid for thinning (and final surfacing) at 5 keV and 10 pA. During TEM analysis, each of the samples were imaged at an acceleration voltage of 200 keV and normally obtained EDS data (Supplementary Table 3) for 1 minute.

#### fO<sub>2</sub> and partitioning coefficient

Because of H escape during decompression, we estimated the molar ratio between Fe and H from the known relationship between unit-cell volume and hydrogen content  $^{33}$ . The estimation shows that H/Fe was close to 1 at high-pressure and 300 K conditions. At high-pressure and 300 K conditions, our measured unit-cell volume of the B2-type FeSi phase was consistent with Fe $_{0.8}\mathrm{Si}_{0.5}$  (Extended Data Fig. 4). Therefore, we assume that the molar ratio of metallic liquid was close to Fe:Si:H = 2:1:1. Note that the (pure) body-centered cubic (bcc) Fe phase was observed after pressure release to 1 bar.

Although the activity coefficients  $(\gamma)$  of Fe in metallic melt  $(\gamma_{\rm Fe}^{\rm met})$  and FeO in the silicate melt  $(\gamma_{\rm FeO}^{\rm met})$  are unlikely to be 1 at 300 K and high-temperature conditions, we assume  $a_{\rm Fe}^{\rm met} = X_{\rm Fe}^{\rm met}$  and  $a_{\rm FeO}^{\rm sil} = X_{\rm FeO}^{\rm met}$  (where a is activity,  $X_{\rm FeO}^{\rm sil}$  is the mole fraction of FeO in silicate melt and  $X_{\rm FeO}^{\rm met}$  is the mole fraction of Fe in metallic melt), because they  $(\gamma_{\rm Fe}^{\rm met}$  and  $\gamma_{\rm FeO}^{\rm sil})$  are not well known at the P–T conditions of this study. In Fe–Si alloys, Si was preferentially oxidized and therefore  $X_{\rm FeO}^{\rm sil}$  is very low (we consider  $\gamma_{\rm FeO}^{\rm sil}$  would not affect and change with this low FeO concentration; Supplementary Table 3). In addition, activity coefficients may become unity at high-temperature conditions (although the effect of high pressure is unknown)<sup>73</sup>, simplified to the oxygen fugacity  $(fO_2)$  relative to Fe–FeO ( $\Delta$ IW) buffer =  $2\log_{10}\left(\frac{X_{\rm PeO}^{\rm int}}{X_{\rm PeO}^{\rm int}}\right)$ . The partitioning coef-

ficient (*D*) of silicon between the metallic melt and the silicate melt is calculated from  $D_{\text{Si}}^{\text{met/sil}} = \frac{X_{\text{Si}}^{\text{met}}}{X_{\text{Si}}^{\text{sil}}}$ , where  $X_{\text{Si}}^{\text{met}}$  is the mole fraction of Si in the

metallic melt and  $X_{SiO_2}^{sil}$  is the mole fraction of  $SiO_2$  in the silicate melts.

# $fO_2$ estimation for the recovered samples

For the EDS measurement in TEM, we selected two regions where the quenched metallic melt and silicate melt are in contact (Fig. 3a,e). Silicate shows a MgO/SiO<sub>2</sub> molar ratio of approximately 1.1 (Supplementary Table 3), which deviates from what is expected for MgSiO<sub>3</sub> bridgmanite. Considering that both the chemical homogeneities of the silicate region near the quenched metallic melt and the molar ratio of MgO and SiO<sub>2</sub>, we interpret that the silicate region represents silicate melt in equilibrium with iron-rich melt during heating. Additionally, according to previously reported melting temperature of hydrous silicates up to 100 GPa<sup>74</sup>, silicates in our high-temperature runs experienced melting.

Assuming that the metallic melt and its surrounding silicate region was locally equilibrated, the  $fO_2$  relative to  $\Delta$ IW buffer can be calculated from  $\Delta$ IW =  $2\log_{10}\left(\frac{X_{\rm Fe}^{\rm int}}{X_{\rm Fe}^{\rm int}}\right)$ , where  $X_{\rm Fe}^{\rm sil}$  and  $X_{\rm Fe}^{\rm met}$  are the mole fraction of FeO in the silicate melt and the mole fraction of Fe in the metallic melt, respectively. These values can be obtained from our chemical measurements. For the same spots, we calculated the partitioning coefficient of silicon between metallic and silicate melts:  $\log_{10}\left(D_{\rm Si}^{\rm met/sil}\right) = \log_{10}\left(\frac{X_{\rm Si}^{\rm met}}{X_{\rm Si}^{\rm sil}}\right)$ 

where  $X_{\rm Si}^{\rm met}$  and  $X_{\rm SiO_2}^{\rm sil}$  are the mole fraction of Si in the metallic melt and the mole fraction of SiO<sub>2</sub> in the silicate melt, respectively (see previous section).

The estimated  $fO_2$  was approximately 4 log units lower than  $\Delta$ IW, that is,  $\Delta$ IW – 4, which is similar to those estimated for the planetary building materials such as chondrites  $^{75}$ . In such a low  $\Delta$ IW value, we observed the large mole fraction of silicon in the metallic region similar to ref. 76. At these reducing conditions, we always observed the following: (1) the formation of FeH and SiO<sub>2</sub>; (2) SiO<sub>2</sub> rather than FeO; and (3) extremely low O content in the metallic melt and silicate region. These observations indicate that the Si in Fe–Si alloys mainly consumed oxygen to form SiO<sub>2</sub>, and Fe combined with H to form FeH rather than FeO.

The partitioning coefficient of silicon between metallic and silicate melts is not well known in a range lower than  $\Delta IW - 3$ . Previous data for the partitioning coefficient of silicon between metallic and silicate melts are mostly plotted higher than  $\Delta IW - 3$  and relatively scattered<sup>73</sup>.

In addition, previous data were obtained under dry conditions<sup>73</sup>. Therefore, it is difficult to compare. Further studies are needed for water effects on the partitioning coefficient of silicon between metallic and silicate melts with a wider range of  $fO_2$ .

#### Stability of a hydrogen-rich layer

We calculated the stability of a layer at the top of the core that formed because of the chemical reaction observed in this study. The mass of the stable layer is  $M_{\rm L} = \left(\frac{4\pi}{3}\right) \rho [R_c^{\ 3} - (R_c - D)^3]$ , where  $R_c = 3,480$  km is the total radius of the core, D is the thickness of the stable layer and  $\rho \approx 10^4$  kg m $^{-3}$  is the density at the top of the core. If the total mass of H transferred across the CMB is  $\Delta M_{\rm H}$ , then approximately  $\Delta M_{\rm Si} \approx k \times \Delta M_{\rm H}$  is the total mass of silicon removed from the core according to the calculation (see next section; k is a simple constant and is calculated in the next section) and reaction observed in this study. Finally, we computed the changes in the weight percentages of H and Si in the stable layer as  $\Delta w_{\rm H} = 100 \times \frac{\Delta M_{\rm H}}{M_{\rm L}}$  and  $\Delta w_{\rm Si} = 100 \times \frac{\Delta M_{\rm Si}}{M_{\rm L}}$ , respectively, where  $M_{\rm L}$  is the total mass of the stable layer.

The density anomalies associated with the addition of H and the depletion of Si in this layer are  $\Delta\rho_{\rm H}$  (negative) and  $\Delta\rho_{\rm Si}$  (positive), respectively. According to first principles calculations (Fig. 3 in ref. 49),  $\Delta\rho_{\rm H}\approx (-1,200~{\rm kg}~{\rm m}^{-3})\cdot\Delta w_{\rm H}$  and  $\Delta\rho_{\rm Si}\approx (-100~{\rm kg}~{\rm m}^{-3})\cdot\Delta w_{\rm Si}$  at the conditions of the CMB. These relations are not sensitive to the exact temperature of the core. The average density anomaly in the layer is thus  $\Delta\rho_{\rm av}=\Delta\rho_{\rm H}+\Delta\rho_{\rm Si}$ , which is always negative given the relative proportions of H and Si that are inferred to move across the CMB via the observed reaction.

We assumed that the density anomaly varies linearly within the stable layer. By definition, the density anomaly is 0 kg m $^{-3}$  at the base of the layer, which is the top of the convective region in the outer core. The density anomaly should then reach a value of  $2\Delta\rho_{\rm av}$  at the CMB. The anomalous density gradient relative to the well-mixed, adiabatic gradient in the core is thus  $\frac{{\rm d}\Delta\rho}{{\rm d}r}=\frac{2\Delta\rho_{\rm av}}{D}(r$  is the radial distance from Earth's centre), which is a negative quantity that increases in magnitude as the layer becomes thinner and/or as more hydrogen enters the layer. Finally, we can calculate  $T_{\rm BV}$  for the stable layer:

$$T_{\rm BV} = 2\pi \left(-\frac{g}{\rho} \frac{\partial \Delta \rho}{\partial r}\right)^{-\frac{1}{2}}$$

which is the period of the vertical oscillations that a fluid parcel would experience if it were perturbed upwards or downwards in the stable layer. Small  $T_{\rm BV}$  corresponds to rapid oscillations and thus strong stratification. Here,  $g \approx 10.7~{\rm m\,s^{-2}}$  is the gravitational acceleration near the CMB.

# Effect of chemical exchange between H and Si on the properties of the topmost outer core

We estimated the amount of Si extracted from the outer core due to the chemical reaction between the core materials (for example, Fe–Si alloys) and the delivered water through a subducting slab. If Si is the most abundant light element in the outer core, O in the delivered water will be consumed for oxidizing Si as below according to this study:

$$Si^{0}(metal) + 2H_{2}O \rightarrow 4H^{0}(metal) + SiO_{2}$$
 (1)

Therefore, the extracted amount of Si at the E'layer,  $\Delta m(Si)_{E'layer'}$  satisfies the following relation:

$$\frac{\Delta m(\mathrm{Si})_{\mathrm{E}/\mathrm{layer}}}{m(\mathrm{Si})} : \frac{m(\mathrm{water}) \times \frac{m(\mathrm{O})}{m(\mathrm{H}_2\mathrm{O})}}{m(\mathrm{O})} = 1 : 2$$
 (2)

where m(Si), m(O) and  $m(H_2O)$  are the molar masses of Si, O and H<sub>2</sub>O, respectively, because Si is extracted as  $SiO_2$  (equation (1)). Thus,  $\Delta m(Si)_{E:laver}$  can be expressed as:

$$\Delta m(Si)_{\text{E-layer}} = \frac{1}{2} \times m(\text{water}) \frac{m(Si)}{m(\text{H}_2\text{O})}$$
(3)

The dissolved amount of H at the E'layer,  $\Delta m(H)_{E'layer}$ , can be also estimated from:

$$\Delta m(H)_{\text{E-layer}} = m(\text{water}) \times \frac{2 \times m(H)}{m(H_2O)}$$
 (4)

where m(H) is the molar mass of H and m(water) is the amount of delivered water at the CMB. The m(water) can be estimated from:

$$m(\text{water}) = C(x) \times \int_{0}^{\Delta t} F(H_2O)(t) dt \approx C(x) \times F(H_2O) \times \Delta t$$
 (5)

where C(x) is an amount of water reacting with the outer core materials at the CMB divided by the water amount subducted at the surface (for example, 0.4–1%),  $F(\mathrm{H_2O})$  is an annual input of water of  $10^{12}\,\mathrm{kg}$  (ref. 12) and  $\Delta t$  is  $2.5\times10^9$  years (that is,  $2.5\,\mathrm{Gyr}$ ). We note that the time-dependent term,  $F(\mathrm{H_2O})(t)$ , is assumed to be constant as it is not well known.

In summary, a ratio in the mass exchange between Si and H at the E'layer, k, can be estimated from:

$$\Delta m(Si)_{E/laver} = -k \times \Delta m(H)_{E/laver}$$
 (6)

The value k is:

$$k = -\frac{1}{4} \times \frac{m(\text{Si})}{m(\text{H})} \tag{7}$$

and therefore approximately -7 (that is,  $-7 \times \Delta m(H) = \Delta m(Si)$  in wt%; that is, combine equations (3)–(6) to make equation (7)). For example, a  $\sim$ 0.002 wt% H increase can decrease Si by  $\sim$ 0.014 wt% from the H–Si exchange. In order to estimate effect on seismic velocity, we assumed that (1) the thickness of the E' layer is 100 km; (2) C(x) is 1%; and (3) velocity changes with elemental concentration follow those reported in refs. 5,51. For Fe–0.81wt%H $^{51}$ , Vp is  $^{-8}$ .29 km s $^{-1}$  at 150 GPa and 4,000 K. At the same P–T conditions, Vp for Fe–1.22wt%H is  $^{-8}$ .47 km s $^{-1}$ . For the Fe–Si system $^{5}$ , a 1 wt% decrease in Si results in a  $^{-2}$ .7% decrease in Vp.

We also calculated how much bulk sound velocity can be changed by the H–Si exchange for hexagonal close-packed (hcp) Fe–Si–H. Using the parameters and methods in the main article (and Supplementary Text 1) in ref. 52, including the combined effects of Si and H, the H increase and Si decrease by the reaction we discussed in the main text (Fe $_{0.9110}$ Si $_{0.0890}$ H $_{0.0010}$ to Fe $_{0.9115}$ Si $_{0.0885}$ H $_{0.0020}$ ) results in a ~0.01% decrease in the bulk sound velocity of Fe–Si–H alloy at 140 GPa.

### **Data availability**

All data supporting this study are available at https://zenodo.org/record/8404634 or by contacting the corresponding authors.

# Code availability

Codes to reproduce the results are available at https://zenodo.org/record/6383505#.YjlacE3P1D8.

## References

- McKelvy, M. J. et al. Exploration of the role of heat activation in enhancing serpentine carbon sequestration reactions. *Environ.* Sci. Technol. 38, 6897–6903 (2004).
- 63. Deschamps, F. et al. Geochemistry of subduction zone serpentinites: a review. *Lithos* **178**, 96–127 (2013).
- Prakapenka, V. B. et al. Advanced flat top laser heating system for high pressure research at GSECARS: application to the melting behavior of germanium. *High Press. Res.* 28, 225–235 (2008).

- Liermann, H.-P. et al. The Extreme Conditions Beamline P02.2 and the Extreme Conditions Science Infrastructure at PETRA III. J. Synchrotron Rad. 22, 908–924 (2015).
- Konôpková, Z. et al. Laser heating system at the Extreme Conditions Beamline, PO2.2, PETRA III. J. Synchrotron Rad. 28, 1747–1757 (2021).
- 67. Boehler, R. High-pressure experiments and the phase diagram of lower mantle and core materials. *Rev. Geophys.* **38**, 221–245 (2000).
- Shen, G. et al. Laser heated diamond cell system at the Advanced Photon Source for in situ X-ray measurements at high pressure and temperature. Rev. Sci. Instrum. 72, 1273–1282 (2001).
- 69. Benedetti, L. R. & Loubeyre, P. Temperature gradients, wavelength-dependent emissivity, and accuracy of high and very-high temperatures measured in the laser-heated diamond cell. *High Press. Res.* **24**, 423–445 (2004).
- 70. Prescher, C. & Prakapenka, V. B. DIOPTAS: a program for reduction of two-dimensional X-ray diffraction data and data exploration. *High Press. Res.* **35**, 223–230 (2015).
- Dorogokupets, P. I. & Dewaele, A. Equations of state of MgO, Au, Pt, NaCl-B1, and NaCl-B2: internally consistent high-temperature pressure scales. *High Press. Res.* 27, 431–446 (2007).
- 72. Shim, S.-H. PeakPo a Python software for X-ray diffraction analysis at high pressure and high temperature. *Zenodo* https://doi.org/10.5281/zenodo.810200 (2017).
- Gessmann, C. K. et al. Oxygen fugacity dependence of Ni, Co, Mn, Cr, V, and Si partitioning between liquid metal and magnesiowüstite at 9–18 GPa and 2200 °C. Geochim. Cosmochim. Acta 63, 1853–1863 (1999).
- 74. Walter, M. J. et al. The stability of hydrous silicates in Earth's lower mantle: experimental constraints from the systems  $MgO-SiO_2-H_2O$  and  $MgO-Al_2O_3-SiO_2-H_2O$ . Chem. Geol. **418**, 16–29 (2015).
- 75. Righter, K. et al. Redox processes in early Earth accretion and in terrestrial bodies. *Elements* **16**, 161–166 (2020).
- 76. Vogel, A. K. et al. The dependence of metal-silicate partitioning of moderately volatile elements on oxygen fugacity and Si contents of Fe metal: implications for their valence states in silicate liquids. *Geochim. Cosmochim. Acta* **237**, 275–293 (2018).
- Robie, R. A. et al. Thermodynamic properties of minerals and related substances at 298.15 K and 1 bar (10<sup>5</sup> Pascals) pressure and at higher temperatures. U. S. Geol. Surv. Bull. 1452, 298–310 (1978).
- 78. Dewaele, A. et al. Quasihydrostatic equation of state of iron above 2 Mbar. *Phys. Rev. Lett.* **97**, 215504 (2006).
- Dobson, D. P. et al. The equation of state of CsCl-structured FeSi to 40 GPa: implications for silicon in the Earth's core. Geophys. Res. Lett. 30, 2002GL016228 (2003).
- 80. Sata, N. et al. Compression of FeSi, Fe<sub>3</sub>C, Fe<sub>0.95</sub>O, and FeS under the core pressures and implication for light element in the Earth's core. *J. Geophys. Res.* **115**, BO9204 (2010).
- 81. Geballe, Z. M. & Jeanloz, R. Solid phases of FeSi to 47 GPa and 2800 K: new data. *Am. Mineral.* **99**, 720–723 (2014).

## **Acknowledgements**

Y.L., T.K. and J.L. were supported by the Leader Researcher programme (NRF-2018R1A3B1052042) of the Korean Ministry of Science and ICT (MSICT). S.-H.S. and T.K. were supported by NSF grants EAR1338810, EAR2019565 and AST2108129. They were also supported by National Aeronautics and Space Administration (NASA) grant 80NSSC18K0353. S.-H.S. also benefited from collaborations and information exchange within the Nexus for Exoplanet System Science (NEXSS) research coordination network sponsored by NASA's Science Mission Directorate. This research used resources of the Advanced Photon Source, a US Department of Energy (DOE) Office of Science User Facility operated for the DOE Office

of Science by Argonne National Laboratory under contract no. DE-ACO2-06CH11357. We acknowledge the support of GSECARS (Sector 13), which is supported by the National Science Foundation—Earth Sciences (EAR-1634415), and the Department of Energy, Geosciences (DE-FG02-94ER14466). Parts of this research were carried out at the PO2.2 beamline at PETRA III, and we acknowledge Deutsches Elektronen-Synchrotron (DESY, Hamburg, Germany), a member of the Helmholtz Association HGF, for the provision of experimental facilities. We also acknowledge the scientific exchange and support of the Center for Molecular Water Science (CMWS) at DESY. We acknowledge resources and support from the Goldwater Environmental Laboratory, part of the Chemical and Environmental Core Facilities at Arizona State University (ASU). We also thank A. Chizmeshya at ASU for providing the synthetic lizardite.

# **Author contributions**

T.K., J.L. and S.-H.S. performed the experiments, and T.K. analysed the X-ray diffraction, SEM, TEM and EDS data. S.C., V.P., R.J.H., N.G. and H.-P.L. supported synchrotron beamline setups and operations. J.G.O. performed the calculations. Y.L. and S.-H.S. supervised the research, discussed the results with T.K. and worked on the manuscript with all authors.

# **Competing interests**

The authors declare no competing interests.

#### **Additional information**

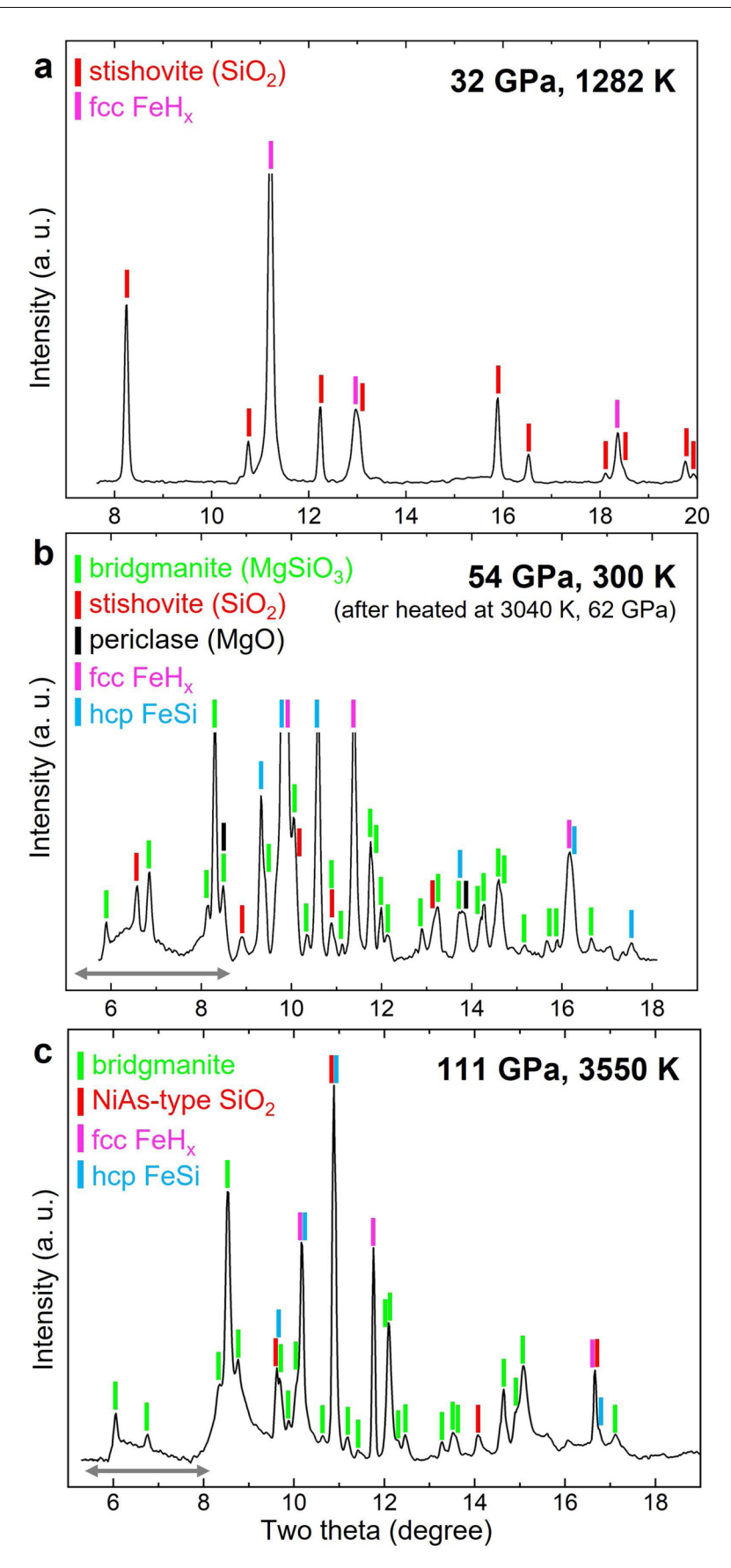
**Extended data** is available for this paper at https://doi.org/10.1038/s41561-023-01324-x.

**Supplementary information** The online version contains supplementary material available at https://doi.org/10.1038/s41561-023-01324-x.

**Correspondence and requests for materials** should be addressed to Sang-Heon Shim or Yongjae Lee.

**Peer review information** *Nature Geoscience* thanks Riko Iizuka-Oku and the other, anonymous, reviewer(s) for their contribution to the peer review of this work. Primary Handling Editors: Alison Hunt and Louise Hawkins, in collaboration with the *Nature Geoscience* team.

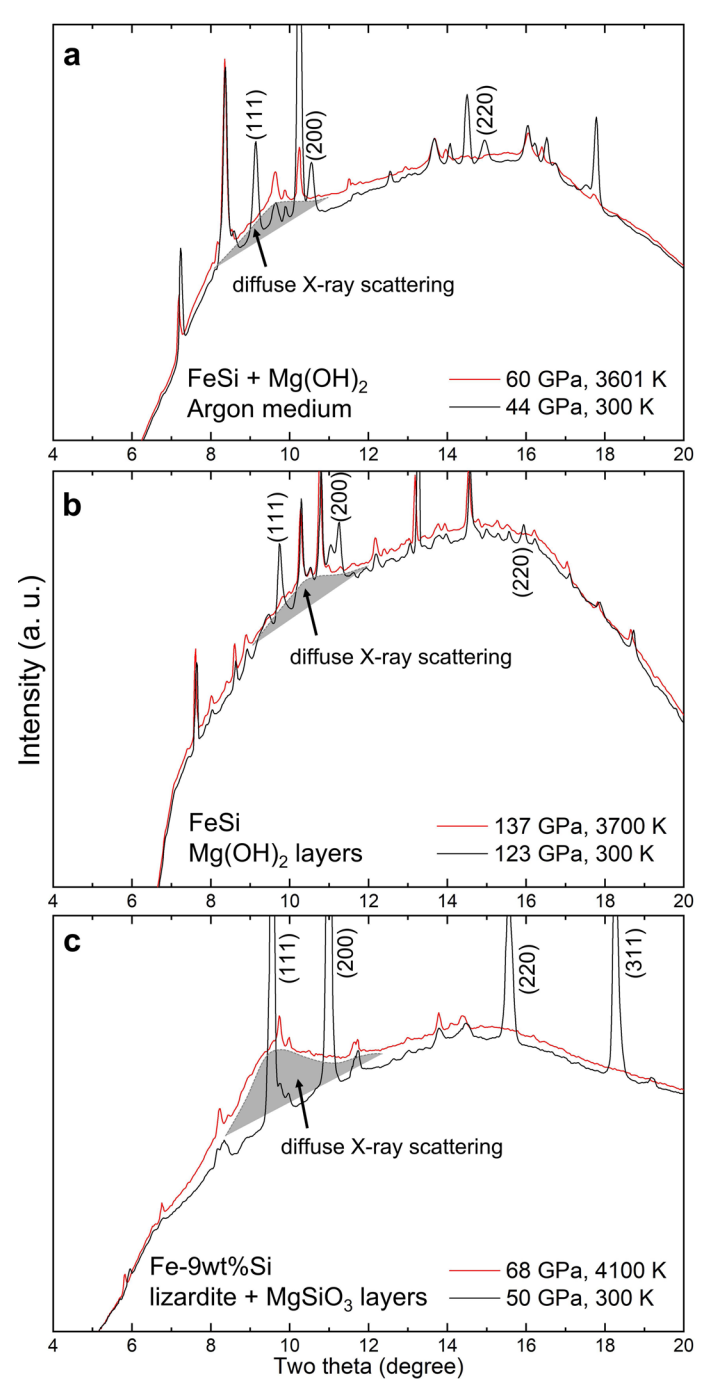
**Reprints and permissions information** is available at www.nature.com/reprints.



Extended Data Fig. 1 | See next page for caption.

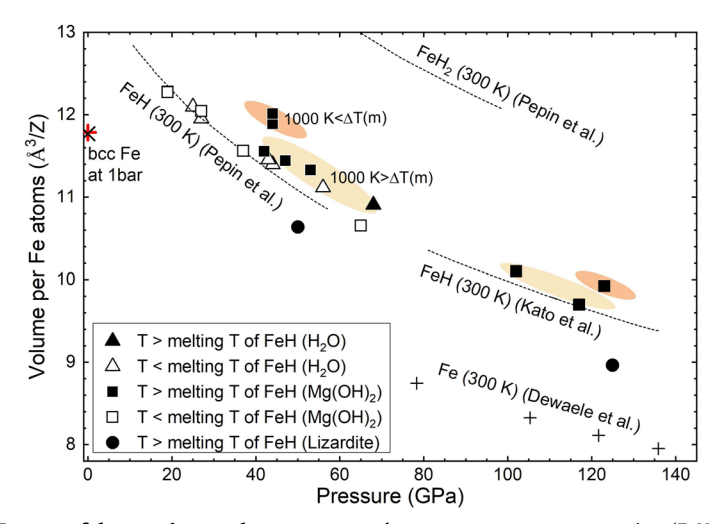
Extended Data Fig. 1 | X-ray diffraction patterns showing the reaction products from a, FeSi in a  $\rm H_2O$  medium (setup 1), b, Fe-9wt%Si sandwiched between hydrous silicate layers (setup 5), and c, Fe-9wt%Si sandwiched between hydrous aluminous silicate layers (setup 6). X-ray diffraction patterns were collected (a) at 32 GPa and 1282 K (A30A\_14), and (b) after temperature

quenching from 3040 K at 62 GPa (A15H\_18), and (c) at 111 GPa and 3550 K (A15I\_29). The X-ray energy was 30 keV for (a) and 37 keV for (b) and (c). The vertical colour bars indicate the positions of the diffraction peaks from the identified phases. The background feature indicated by a double-sided grey arrow in low two-theta region in patterns (b) and (c) is from laser carbon mirrors.



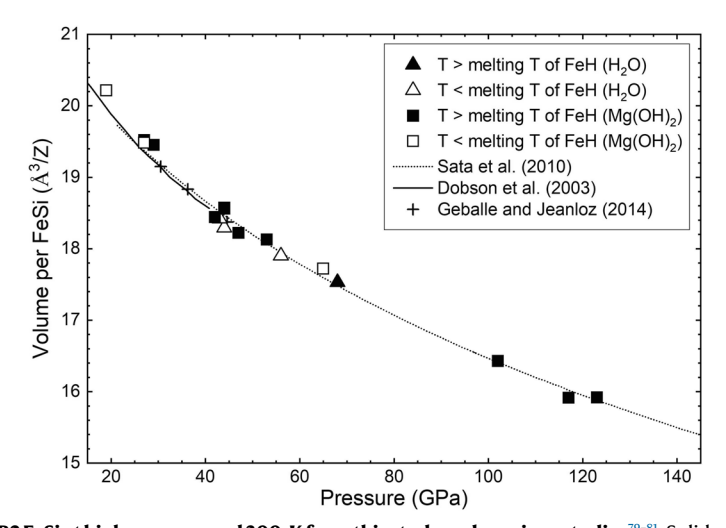
Extended Data Fig. 2 | In situ X-ray diffraction patterns measured during laser heating (a, 60 GPa and 3601 K (A30B\_36), b, 137 GPa and 3700 K (A15G\_28), and c, 68 GPa and 4100 K (A15H\_26)) and after temperature quenching (44 GPa and 300 K (a), 123 GPa and 300 K (b), and 50 GPa and 300 K (c)).

In the high-temperature patterns, the broad diffuse X-ray scattering mainly from FeH  $_{\!x}$  melt is highlighted by grey-shaded area. The diffraction peaks of fcc FeH  $_{\!x}$  (with Miller indices) were observed only after temperature quench to 300 K.

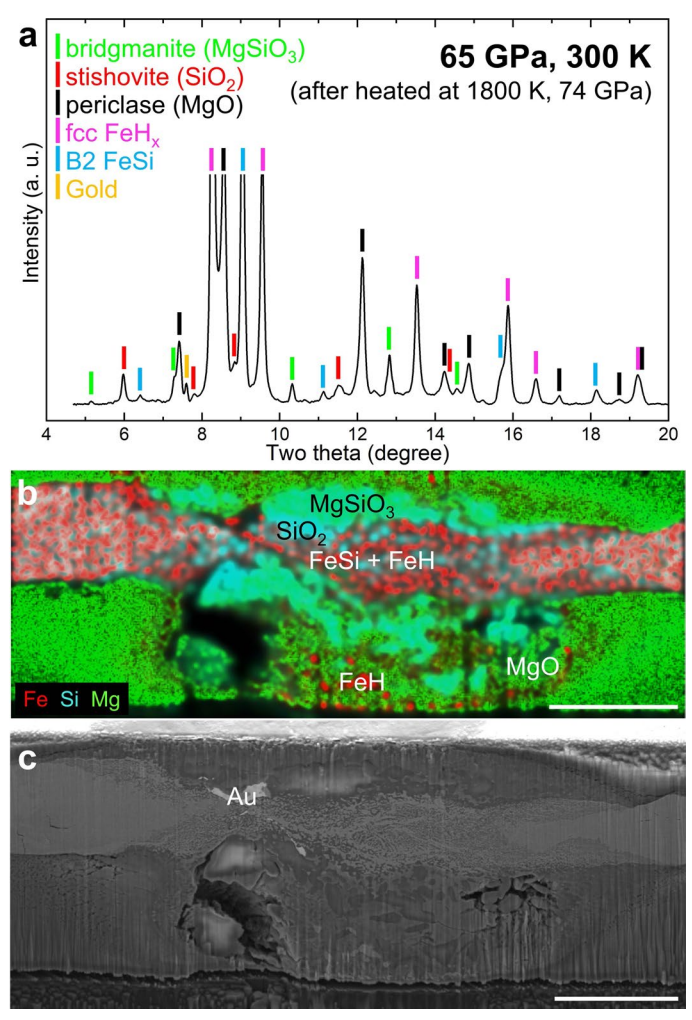


Extended Data Fig. 3 | The volume per Fe atom of the reaction product, FeH<sub>x</sub>, after heating at 300 K. Solid and open symbols indicate temperature (T) conditions were higher than melting T of FeH<sub>x</sub> or lower than melting T of FeH<sub>x</sub>, respectively. The volume of bcc Fe at 1 bar, measured from FeSi +  $\rm H_2O$  setup after heating and pressure released 1 bar, is shown as a red cross. Previous results are

shown as separate curves or points (FeH and FeH $_2$  (300 K) $^{35}$ ; FeH (300 K) $^{36}$  for higher pressure; bcc Fe $^{77}$  (black cross at 1 bar); hcp Fe $^{78}$  (black crosses at high pressures)).  $\Delta$ T(m) is a temperature difference between the measured T during heating and the melting temperature of fcc FeH $^{37}$ .

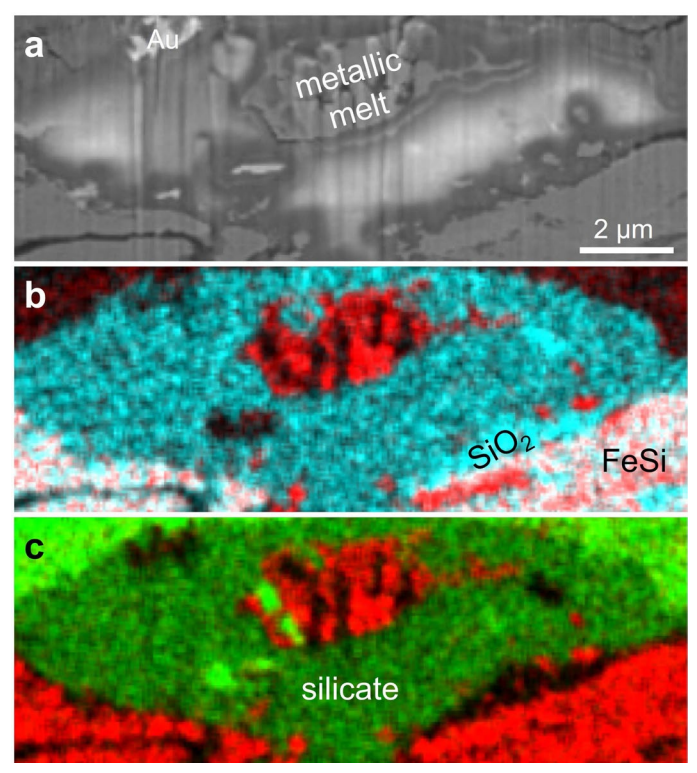


 $\textbf{Extended Data Fig. 4} | \textbf{The volumes of B2 FeSi at high pressure and 300} \ \ \textbf{K from this study and previous studies}^{79-81}. \\ \textbf{Solid and open symbols indicate temperature conditions were higher than melting T of FeH}^{37} \text{ or lower than melting T of FeH, respectively.}$ 

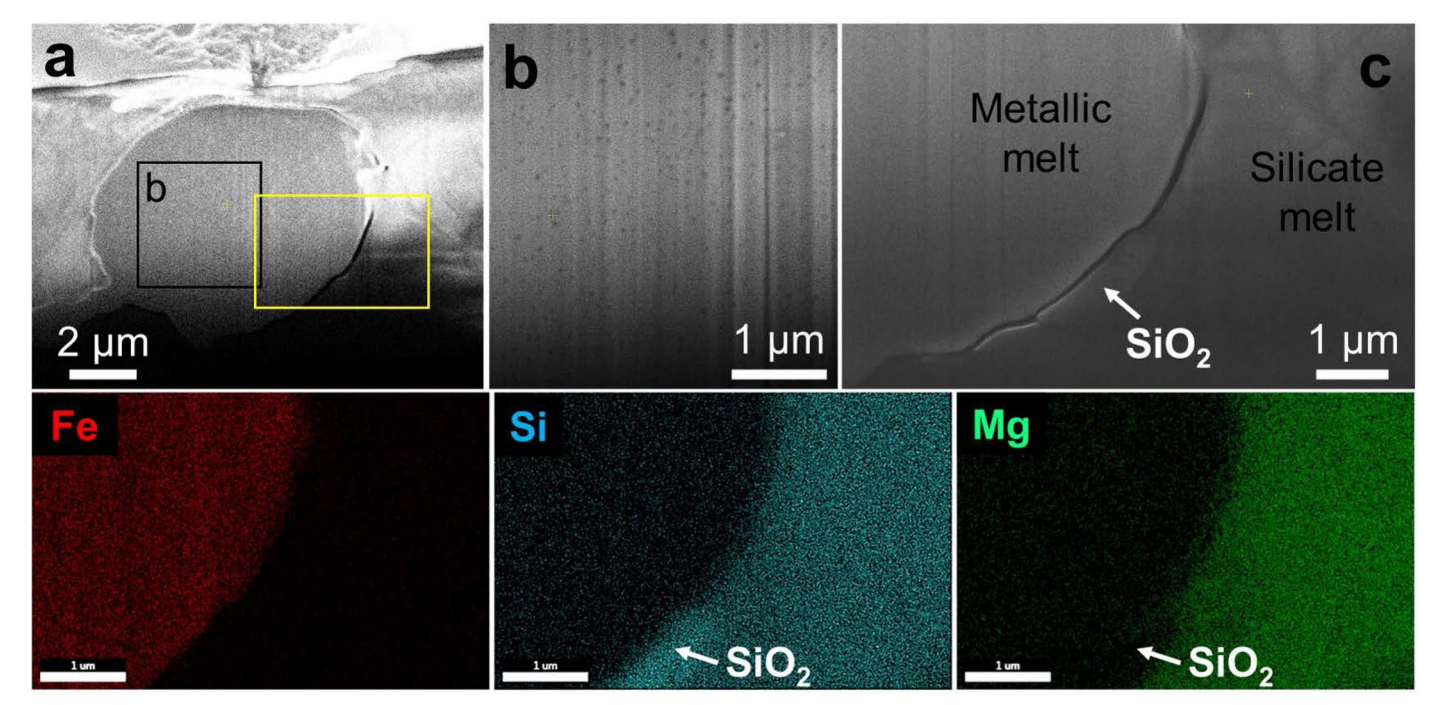


Extended Data Fig. 5 | XRD pattern and SEM analysis of the recovered sample from laser heating of Fe-9wt%Si sandwiched between two  $Mg(OH)_2$  layers. a, In situ X-ray diffraction pattern, and b, c, chemical analysis obtained from

experiments at 65 GPa and 300 K after heated at 1800 K at 74 GPa (P30A\_18). The experimental setup was a Fe-9wt%Si foil sandwiched between Mg(OH) $_2$  layers. The scale bars are 7  $\mu$ m.

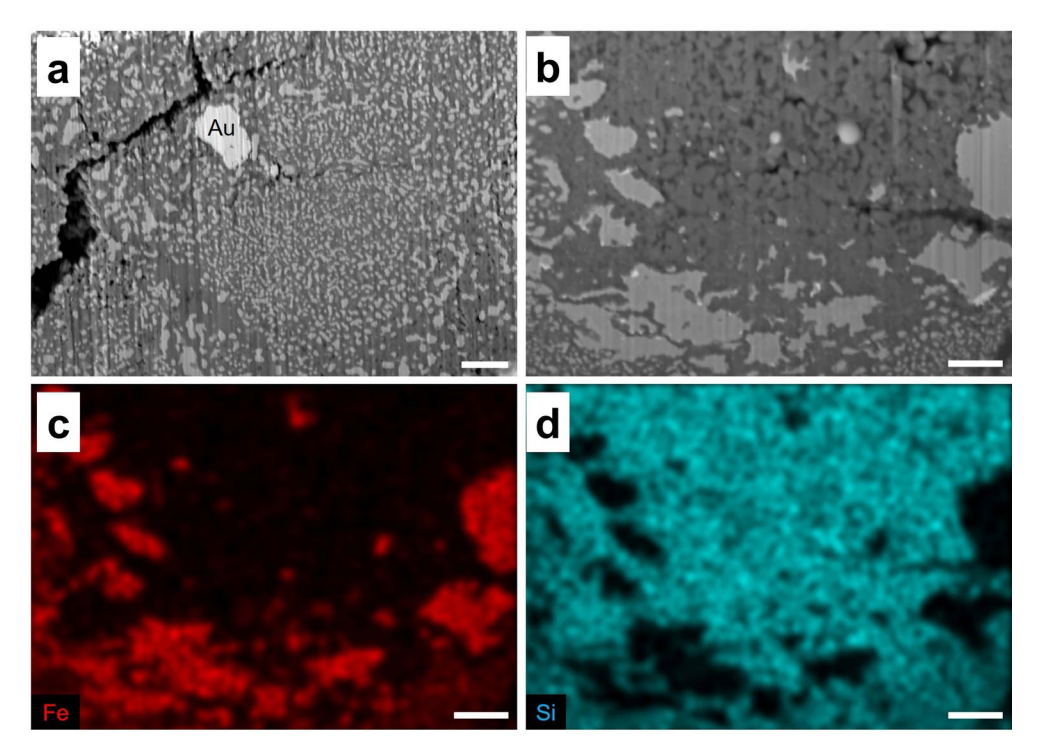


Extended Data Fig. 6 | SEM analysis of the recovered sample from laser heating of FeSi sandwiched between two  $Mg(OH)_2$  layers. a, A cross-sectional view of the recovered sample after heating at 2810 K and 129 GPa (A15G\_18). The two-dimensional elemental distribution maps of b, Fe (red) and Si (cyan), and c, Fe (red) and Mg (green).



Extended Data Fig. 7 | SEM-EDS analysis of the recovered sample from laser heating to 4100 K at 68 GPa of Fe-9wt%Si sandwiched between two Lizardite+MgSiO\_3 layers (setup 5). a, An SEM image of the cross-section of the recovered hot spot (A15H\_26). b, The porous texture at the centre of metallic melt (the black box in a) indicates hydrogen escaped from the metallic melt upon

decompression to 1 bar. c, An SEM image of the boundary between the metallic melt and silicate melt. The bottom row shows elemental distribution maps for Fe, Si and Mg obtained for the yellow box in (a). The  $SiO_2$  grain was produced by the reaction between Si from the Fe-Si alloy and water from silicate at the boundary between metallic melt and silicate melt.



Extended Data Fig. 8 | SEM images of the recovered samples from FeSi +  $H_2O$ . a, The centre of the heated spot after quenching from 1282 K at 32 GPa (A30A\_14). b, The centre of the heated spot after quenching from 1202 K at 28 GPa (A30A\_09). Elemental distributions of c, Fe, and d, Si of the area in (b). When

 $H_2O$  medium was used, the recovered samples showed complete conversion of FeSi alloy to  $SiO_2$  and FeH, which also agrees with in situ X-ray diffraction result (Extended Data Fig. 1a). The cracks in (a) are caused by decompression. The scale bars are  $1\,\mu m$ .